8

Thermoelectric Nanocomposite for Energy Harvesting

Ehsan Ghafari[1], Frederico Severgnini[2], Seyedali Ghahari[1], Yining Feng[1], Eu Jin Lee[3], Chaoyi Zhang[1], Xiaodong Jiang[1], and Na Lu[1, 4]

[1] *Purdue University, Lyles School of Civil Engineering, Department of Civil Engineering, SMART Laboratory, Stadium Avenue, West Lafayette, IN 47906, USA*
[2] *Purdue University, School of Electrical and Computer Engineering, Northwestern Avenue, West Lafayette, IN 47907, USA*
[3] *Purdue University, School of Chemical Engineering, Stadium Avenue, West Lafayette, IN 47907, USA*
[4] *Purdue University, Birck Nanotechnology Center, State Street, West Lafayette, IN 47907, USA*

8.1 Introduction

Each year nearly 60% of energy produced in the United States is lost as waste heat. Among them 20–50% waste heat is generated from industrial process, such as power plants, metal furnaces, and chemical productions. Figure 8.1 shows the 2015 energy flowchart released by Lawrence Livermore National Laboratory, which details the sources of energy production and energy consumptions. In the US manufacturing sector alone, more than 3000 TW of waste heat energy is lost each year, which is equivalent to more than 1.72 billion barrels of oil [1, 2]. Those waste heat can be directly converted to electricity using thermoelectric (TE) devices via Seebeck effect [3]. Also the increasing consumption of fossil fuels has led to severe environmental issues recently, such as global warming, ozone depletion, and atmospheric pollution [4]. Additionally, the fast development of the industry has caused energy shortages all over the world. The overall energy demand of the world has never stopped climbing. Thus, a new generation of high-performance and cost-effective TE materials would make significant impacts on meeting the challenge of increasing energy demands in the future. The TE devices are a promising renewable energy technology because these solid-state devices can directly convert heat given off from sources such as power plants, factories, motor vehicles, computers, or even human bodies into electrical energy without using toxic chemicals and moving parts [5–8]. Conversely, the TE devices can also convert electrical energy into thermal energy for cooling or heating through Peltier effect. However, the low efficiency of current TE devices causes the limited commercial application. Figure 8.2 depicts the potentials of using TE devices for power generation and shows the different scales of energy generation that are relevant to different applications [9]. Therefore, the development of high-performance TE materials becomes a promising

Multifunctional Nanocomposites for Energy and Environmental Applications, First Edition.
Edited by Zhanhu Guo, Yuan Chen and Na Luna Lu.

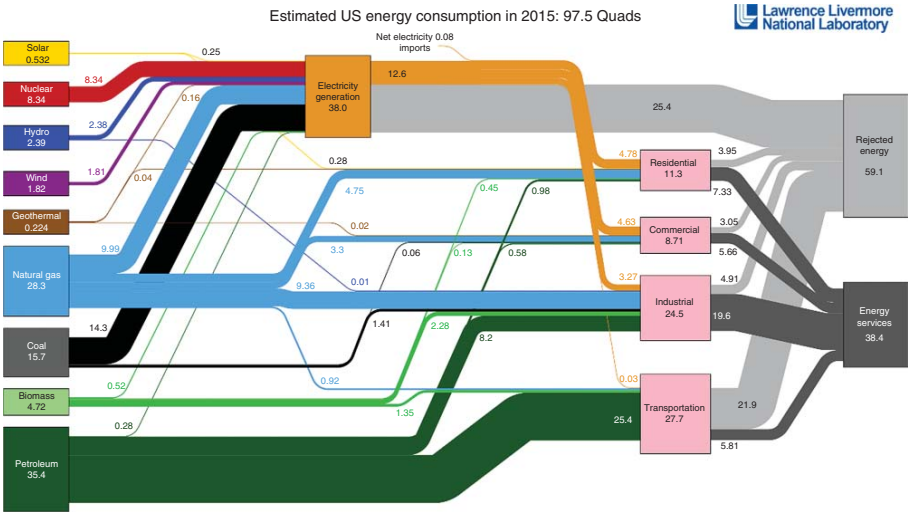

Figure 8.1 The 2015 energy flowchart released by Lawrence Livermore National Laboratory. (Chen *et al*. 2012 [1]. Reproduced with permission of Elsevier.)

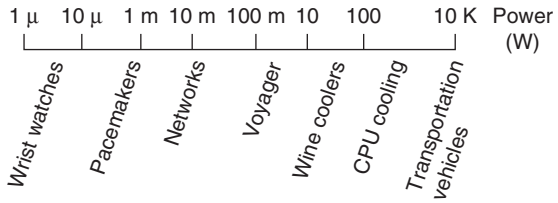

Figure 8.2 The potential power generation. (Pichanusakorn and Bandaru 2010 [9]. Reproduced with permission of Elsevier.)

approach for waste heat recovery. The high-efficiency TE materials are important waste heat recovery systems, such as thermoelectric generator (TEG) that converts waste heat into electrical energy. The conversion of waste heat into electricity has a significant impact on the energy technology to help us reduce the dependence on fossil fuels and to solve the environmental issues.

The term "thermoelectric effect" came into existence around mid-nineteenth century. Thomas Johann Seebeck was one of the pioneers of TE technology. A son from a rich Baltic German family hailing from Reval or modern-day Estonia, he gave up a profession in medicine to study physics where his true passion lied [10]. He first discovered in 1821 the relationship of direct conversion between the temperature differences and electric voltage. This effect was named after him because he observed it through an experiment, which has a circuit consisting of two metals that when one end was heated, a TE-induced current would deflect the compass needle. It was initially thought that the compass deflection was caused by magnetism induced by a temperature difference and was related to the Earth's magnetic field. However, he soon realized that it was in fact due to something, which he coined as a "thermoelectric force" that created an electric current that by Ampere's law caused the deflection [11].

About 13 years later, in 1834, a former watchmaker and dealer who later became a physicist, Jean Charles Athanase Peltier found that electrical currents could be produced by heating and cooling at the junction of two dissimilar metals [12]. In 1838 a Russian physicist by the name of Heinrich Lenz discovered that depending on the direction of the current, by removing heat from the junction, it could freeze water into ice while reversing the direction of the current it would instead melt the ice. The proportionality constant between electric current and the heat absorbed or created at the junction was known as the Peltier coefficient, or the amount of heat carried through a system per unit charge [13]:

$$Q = (\pi_A - \pi_B)\, I \tag{8.1}$$

where Q was the heat generated at the junction per unit time. It was equal to the Peltier coefficient of conductors A and B ($\pi_A - \pi_B$) and I was the electrical current passing through the junction. Peltier realized that if the π_A and π_B were different, a continuous flow of current had to be supplied across the junction, or else a discontinuity would arise from the heat flow. This equation provided the basis for explaining why some junctions in a heat pump device that Peltier created consisting of multiple junctions would lose heat due to the Peltier effect, while others gain heat. This phenomenon is exploited in many TE cooling devices in refrigerators [14]. The close relationship between Peltier and Seebeck effects can be expressed as $\pi = TS$, which was later established by Lord Kelvin, who

explained the correlation between the Seebeck and Peltier effects also known as the Kelvin Relations. He found that the effects were related by thermodynamics, which lead him to discover the third TE effect, which is now known as the Thompson effect [15]. The Peltier effect can be considered as the reverse reaction to the Seebeck effect (analogous to the back-emf in magnetic induction): if a simple TE circuit is closed, then the Seebeck effect would drive a current, which in turn (via the Peltier effect) will always transfer heat from the hot to the cold junction [16].

In the 1920s–1970s, between the world wars, many brilliant minds were researching the possibility of applying TE technology to harness thermal energy for electricity generation. Research was conducted in hopes that their efforts would bear fruit in a form of groundbreaking technology that could set nations apart from each other. Primarily, the theories of thermoelectricity were used in cooling as well as in power generation for military and civilian uses. In the 1950s, the efficiency of TEGs had reached to 5%, which was able to cool ambient temperature to subzero temperatures. These series of events sparked the interest and research that could ultimately contribute to some viable industries. The possibility of TE technology replacing conventional heat engines and refrigeration excites appliance corporations, such as Westinghouse, universities, and national research laboratories. However, the progress of TE research has been slow since 1960, and the application of TE technology is limited to military and space explorations.

8.2 Fundamental of Thermoelectric Effect

The efficiency of a material for TE applications is determined by a dimensionless quantity ZT, where T is the absolute temperature and Z is

$$Z = \frac{S^2\sigma}{k} \tag{8.2}$$

In this expression, S is the Seebeck coefficient, σ is the electrical conductivity, and k is the thermal conductivity. In physics, k consists of the electronic part (k_e, due to carrier transport) and lattice part (k_{Ph}, due to phonon transport). The term $S^2\sigma$ is called the power factor (PF). A large PF indicates that a large voltage with high current will be generated, whereas a low k is preferred to restrict the energy loss due to the thermal leakage from the hot side to the cold side in a device.

8.2.1 Seebeck Effect

The Seebeck coefficient (S, also referred as thermopower, in volts per kelvin) is an intrinsic material property, which measures the TE voltage induced in response to a temperature difference across the material. In physics, S represents the energy difference between the averaged charge carrier energy versus Fermi energy. Mathematically, it can be expressed as

$$S = \left(\frac{k}{-q}\right)\left(\frac{E_c - E_F}{kT} + \frac{\Delta_n}{kT}\right) \tag{8.3}$$

In this expression, E_F is the Fermi level, which can be mathematically expressed by Eq. (8.4) where the dependence to the temperature (T) and the Boltzmann constant (k) are made explicit. The variable E represents energy and μ is electrochemical potential:

$$f(E) = \frac{1}{1 + e^{\frac{E-\mu}{kT}}} \tag{8.4}$$

As a general rule, electric current exists when charge carriers flow from one point to another. This flow depends on the difference of Fermi levels between the two points. If a given state is occupied by electrons in point A, but states with lower energy are available in point B, the charge will move from A to B to occupy the lower state. When applying a difference of voltage between the two contacts (ΔV_{AB}), the electrochemical potentials between the two ends will be shifted, creating a Fermi window (a difference between two Fermi functions). By doing so, a series of states will be available in B, so the electrons in A with an energy greater than μ_B will flow to B, generating an electric current.

As mentioned before, the Fermi occupation also depends on temperature. The assumption that the occupation will behave like the blue line in Figure 8.3 is not true for higher temperatures. For these cases, the occupation behavior will be changed, as seen in the red and black lines. The red line represents the Fermi function for the material at 293 K and the black, for that at 2000 K.

According to Eq. (8.4), when the energy (E) equals the electrochemical potential μ, $f(E)$ is 0.5, meaning that 50% of the states are filled and 50% are empty. For a

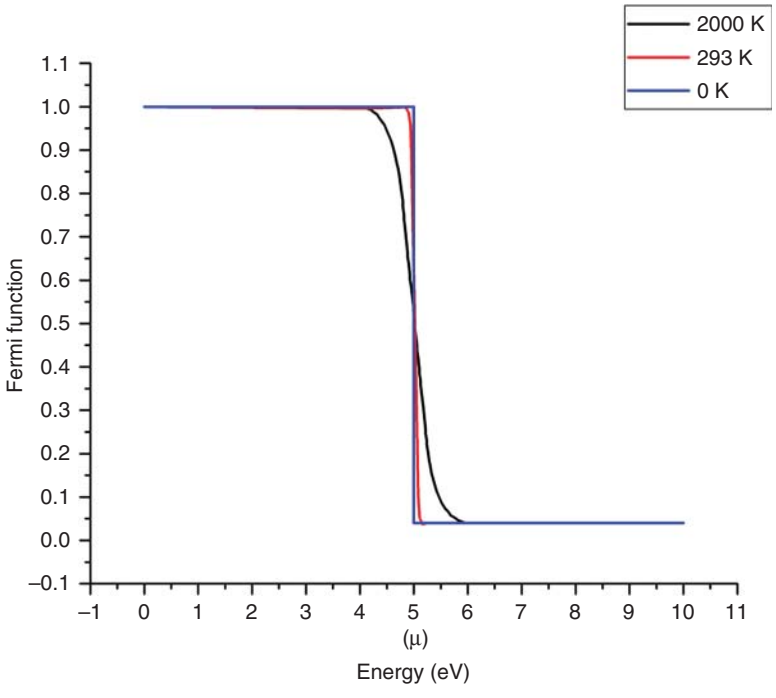

Figure 8.3 Fermi function as a function of energy for different temperatures.

given value of energy above μ, the number of filled states decreases. Conversely, for energies lower than μ, the number of occupied states increases, and $f(E)$ gets gradually closer to 1, meaning that 100% of the states are filled. Therefore, the higher the temperature, the less the distribution resembles a step function, acquiring instead an "S"-shaped curve. This shape implies that, in a hot material, there are more electrons occupying the states with higher energy and less electrons occupying the states with lower energies. Or alternatively, there are more holes at lower energies.

Given the fact that the occupancy factor varies with temperature, what would happen if two samples A (hot) and B (cold) of a semiconductor are connected? A flux of electrons from A to B is expected to happen, since electrons in A have higher energy and can now freely move to lower energy states available in B. Likewise, a flow of holes from A to B will happen, since there are more holes below μ in A than there are in B.

Because there are electrons and holes contributing to opposite flow of currents, the net current flow is zero. This can be seen in semiconductors with no doping, where the density of states (DOS) can be assumed to be constant for short values of energy above and below the Fermi level.

However, a different behavior can be perceived in doped materials. The doping process changes the DOS diagram: in n-type material, DOS grows with energy, while in p-type material it decreases with energy. Both cases are reciprocal, so the understanding of one can be used to determine the behavior of the other. Let us first analyze the n-type case.

For this case, there are more electrons occupying higher states than there are holes occupying the lower states. For this reason, even though n- and p-type carriers are still flowing in the junction, their contributions are different, resulting in a net flow of electrons from A to B (or an electric current from B to A).

In the p-type semiconductor, their contributions are also different, but now the holes are more numerous, so a net flow of holes is expected from A to B (or an electric current from A to B). If A and B are two ends of an open circuit, the net flow of charges will be piled up at the ends of the circuit, creating a potential until a steady state is reached. In this condition, the net flow of charge carriers will be canceled by the voltage at the ends of the terminal. This difference of voltage generated due to a difference in temperature is the Seebeck effect; therefore, the Seebeck coefficient can be given by Eq. (8.5):

$$S = \frac{\Delta V}{\Delta T} \tag{8.5}$$

The Seebeck effect is the core mechanism of thermoelectricity. The investigation of effective approaches to improve S is an exciting and open field. A promising application of a material with high Seebeck coefficient is the possibility of harvesting heat and converting it to electricity, a nontoxic and reliable solution for energy generation. In the Sustainable Materials and Renewable Technology (SMART) Lab at Purdue University, one of the major focuses is the development of cost-effective materials with high Seebeck coefficients that are capable of functioning at higher temperatures to harvest the heat wasted by industrial processes above 800 K for power generation.

8.2.2 Thermal Conductivity

Thermal conductivity is the parameter that describes how efficiently a material can conduct heat. Low thermal conductivity can be seen intuitively as a requirement to maintain a certain temperature gradient [17], which is essential for reaching high ZT in a material system. If the material has a high thermal conductivity, the temperature gradient would quickly turn into a uniform temperature, so the TE phenomena would no longer be observable. In the case of semiconductors, the total thermal conductivity (κ_T) can be given by the sum of two other components, as seen in Eq. (8.6):

$$\kappa_T = \kappa_e + \kappa_l \tag{8.6}$$

In Eq. (8.6), κ_e and κ_l are the electron and lattice thermal conductivity, respectively. κ_l is known as the most important mechanism for heat conduction in semiconductors at temperatures close to room temperature, which normally accounts for 90% of the contributions in wide bandgap materials. However, the contribution of electrons to the heat transport cannot be neglected, due to the following reasons:

1) Semiconductors engineered to work as TE materials are often heavily doped, in order to achieve higher electrical conductivity [17]. Since doping the material increases the number of charge carriers, it naturally increases the total amount of heat that is going to be transferred by these carriers as well. So doping can be an effective strategy to increase the PF in a material, but it also simultaneously increases κ_e.
2) At higher temperatures, κ_e increases to become the dominant mechanism of heat transfer. With an increase in temperature, charge carriers become thermally excited and so they can carry more heat [17]. For this reason, the development of TE materials to operate in higher temperatures must take into consideration the effects due to charge carriers.

The parameters κ_e and κ_l will be detailed separately.

To properly understand the heat conduction mechanism in the lattice, the concept of phonons needs to be discussed. Phonons are seen as lattice vibration that travels throughout the crystal, possessing a specific frequency and wavelength. Accordingly, to the wave-particle duality, the behaviors of phonons can also be seen as a particle and a wave. And just like electrons, they can be described by a dispersion relation. Because the semiconductor crystals are periodic, the phonon dispersion relations are also periodic with respect to the momentum K [18].

The efficiency of heat transfer is related to the phonon's mean free path (MFP), which is a measurement of the average distance the particle can travel in the material without scattering. Because the elements responsible for causing scattering may change with temperature, so does the MFP and, naturally, also κ_l.

At lower temperatures, the scattering between two phonons is weak and the phonon MFP is longer. In this regime, κ_l is proportional to T^3 [17]. This behavior is observed in temperatures up to 10 K and is known as the Casimir regime [19]. For higher temperatures, the impurities present in the semiconductor significantly change the MFP. Bigger impurities are capable of scattering phonons

with higher wavelengths, while smaller impurities scatter phonons with lower wavelengths:

$$\kappa_l = \frac{1}{3} c v \lambda \tag{8.7}$$

In this equation, c is the thermal capacity per cubic centimeter of material, v is the group velocity, and λ is the already established MFP. Of all these factors, only the MFP strongly depends on the temperature. For this reason, κ_l decreases in hotter materials.

Because it is important for TE materials to have low thermal conductivity, the use of nanoparticles to reduce κ_l by increasing phonon scattering is a topic of extensive research. One of the ongoing projects at the SMART Lab in Purdue University involves the use of superlattices and doping impurities of different sizes in TE materials to lower the phonon MFP, without compromising electrical properties [20–22]. By doing so, the thermal conductivity is expected to reduce, while the electrical conductivity will be maintained in a fixed level.

In semiconductors, the total electronic thermal conductivity can be expressed in Eq. (8.8):

$$\kappa_e = \kappa_n + \kappa_p + \kappa_b \tag{8.8}$$

In Eq. (8.8), κ stands for thermal conductivity; n and p denote thermal conductivity due to electrons and holes, respectively. κ_b is the bipolar thermal conductivity, which is given by Eq. (8.9) [17]:

$$\kappa_b = \frac{(\sigma_n \sigma_p)}{S_n - S_p} (S_n - S_p)^2 T \tag{8.9}$$

where S is the Seebeck coefficient and σ is the electric conductivity. At higher temperature, the intrinsic doping of semiconductor is a dominating effect; the bipolar conductivity becomes an important factor. At first glance in Eq. (8.8), we could wrongly conclude that κ_b be directly proportional to the temperature (T). However, it is important to keep in mind that κ_b is also directly proportional to the square of the difference between the Seebeck contributions from electrons and holes, expressed in Eq. (8.9) by the term $(S_n - S_p)^2$, which itself also depends on temperature. For this reason, near the intrinsic regime, the relation between the bipolar thermal conductivity and temperature near the intrinsic regime is not linear. Instead, it can be more accurately described by Eq. (8.10) [23]:

$$\kappa_{bi} \propto \exp\left(-\frac{E_g}{2\kappa_b T}\right) \tag{8.10}$$

The understanding of the bipolar thermal conductivity is necessary to comprehend an important fact of high temperature thermoelectricity. When reaching higher temperatures, the overall κ_T of materials tends to increase, despite the fact that the phonon contribution gets smaller because κ_{bi} reaches a huge values and it becomes a mechanism of heat conduction in the material.

8.2.3 Electrical Conductivity

As seen in Section 2.2, thermal conductivity describes how efficiently a certain material can conduct heat. Likewise, electrical conductivity (σ) describes the ease with which a material conducts charge carrier transport. A high value for σ means that charge carrier (or electric current) can easily flow through the material.

In order to properly understand the dependence of σ to the temperature, let us consider first an electron able to move within a crystal lattice. In an ideal case, this lattice is composed by a certain arrangement of atoms that is periodically repeating itself in a perfect fashion. The moving electron sees each one of these atoms as a potential field, so the lattice itself is a periodic arrangement of potential fields. It is important to have in mind that, due to thermal effects, these atoms are vibrating in the lattice. These potential disturbances are capable of scattering the electron and, by doing so, changing the electron MFP and the electrical conductivity. With higher temperatures, the amplitude of the vibrations will be bigger, and so the potential disturbances will be more intense, thus electron scattering will be more frequent [24].

Using the Landauer approach, σ can be written according to Eq. (8.11) [18]:

$$\sigma = \frac{2q^2}{h} \langle\!\langle \lambda \rangle\!\rangle \langle M/A \rangle \tag{8.11}$$

This equation summarizes several different physical factors that interfere in the charge transport, in a set of simple terms. Here, conductance is defined by the quantum of conductance $\left(\frac{2q^2}{h}\right)$, the average MFP for backscattering $\langle\!\langle \lambda \rangle\!\rangle$, and the average number of channels in the Fermi window M/A. The quantum of conductance is the basic quantized value for conductivity. The average MFP for backscattering is the result of several different phenomena acting together to interfere in the mobility of an electron across the lattice, such as lattice vibrations, chemical bonds, and size of the lattice atoms. The average number of channels is defined as being the ratio of available modes per unit area. It is important to remember that the only channels that should be considered for the conductivity are the ones inside the Fermi window [18]. Putting in other terms, the only channels to be considered are the ones available in the interval of Fermi functions $f_A - f_B$, if A and B are the points where the motion of electron begins and ends.

8.2.4 Figure of Merit

The TE performance of materials is measured as the figure of merit (ZT) [25], which is defined as follows:

$$ZT = \frac{S^2 \sigma T}{\kappa} = \frac{S^2 T}{\kappa \rho} = \frac{S^2 T}{(\kappa_e + \kappa_l)\rho} \tag{8.12}$$

where S is the Seebeck coefficient; σ and κ are the electrical and thermal conductivity, respectively; T is the absolute temperature; ρ is the electrical resistivity; and κ is the thermal conductivity of TE materials, which consists of two parts: lattice thermal conductivity (κ_l) and electronic thermal conductivity (κ_e). The efficiency

of TE device is governed by the Carnot efficiency and material figure of merit ZT as the following Eq. (8.13) [26]:

$$\varepsilon = \frac{T_H - T_C}{T_H}\left(\frac{\sqrt{1+ZT_M}-1}{\sqrt{1+ZT_M}+T_C/T_H}\right) \tag{8.13}$$

where T_H, T_C, and T_M are the hot-side, cold-side, and average temperatures, respectively, and ε_C is the Carnot efficiency and can be expressed as Eq. (8.14):

$$\varepsilon_C = \frac{T_H - T_C}{T_H} \tag{8.14}$$

The coefficient of performance η of a TE couple is given by Eq. (8.15):

$$\eta = \frac{T_C\left(\sqrt{1+ZT}-T_H/T_C\right)}{(T_H - T_C)\left(\sqrt{1+ZT}+1\right)} \tag{8.15}$$

8.3 Historical Perspective of Thermoelectric Materials Development

8.3.1 Early Discovery of Thermoelectricity

The discovery of thermoelectricity happened in the nineteenth century, by the German physicist Thomas Johann Seebeck and the French physicist Jean Charles Athanase Peltier. In the twentieth century, the Russian physicist Abraham Fedorovich Ioffe discovered a series of mechanisms and paradigms related to TE materials. In 1949, Ioffe developed a comprehensive theory of macro- and microscopic thermoelectricity that covered the following points [27]:

1) Introduction of the figure of merit (ZT), as a dimensionless parameter to describe the efficiency of a material for TE conversion
2) Estimation that degenerate semiconductors would be the most promising materials for TE conversion and that optimum doping should be between 5×10^{18} and 1×10^{19} cm^{-3}

This theory was first developed as a classified material. In 1956, Ioffe participated in other publications such as "Semiconductor Thermoelements" and "Thermoelectric Cooling," promoting the theory of thermoelectricity performed by semiconductors to the scientific community.

8.3.2 TE Devices in Post-90

- The current attempt to optimize TE parameters is known as phonon glass electron crystal (PGEC), as suggested by Slack [28]. This approach basically consists of designing materials that poorly conduct phonons (like a glass would) and efficiently conduct electrons (like a crystal lattice). The challenge of this approach is the fact that phonon and electron transport have a certain degree of dependence on each other; for instance, adding dopants to increase electrical conductivity often cause an undesired increase in

thermal conductivity. In order to achieve high figure of merit, nanostructured materials, approach to decouple electron, and phonon transport have been extensively explored recently, which include adding nanoparticles in semiconductors to reduce lattice thermal conductivity by scattering phonons while preserving electron's MFP [29].

- Developing periodic structures of nano-layers of two or more materials (known as superlattices), to enhance cross-plane Seebeck effect and increase phonon scattering to reduce thermal conductivity [30].
- Adding quantum wells in bulk materials, to confine electrons in a narrow 2D gap, aiming to improve carrier mobility.
- Developing more complex unit cells (clathrates and skutterudites) that encapsulate heavier guest atoms, to further reduce thermal conductivity through enhanced phonon scattering [31].

This general idea of using nanotechnology to improve TE performance of materials was first proposed by Prof. Mildred Dresselhaus at MIT, who suggested that quantum confinement effect in low dimensional semiconductors can lead to ZT improvements in TE performance [32].

For space missions where the light from the sun is considerably weak and solar panels cannot perform efficiently, the electrical power is provided by TE couples. Also, near the sun, solar cells would not perform as they are designed to because of the extreme heat and high incident particle flux [33].

The heat is generated from a Pu-238. The device is called radioisotope thermoelectric generator (RTG), and it has been used by NASA in Apollo, Pioneer, Viking, Voyager, Galileo, and Cassini missions. Silicon–germanium (SiGe) TE devices are the main modules that have been used widely for that very purpose in RTGs. SiGe TE couples are heavily doped semiconductors. At high temperatures, such material shows a considerable high figure of merit (ZT) up to 2 [34]. SiGe alloys are malleable, can have a good bonding with the other components, have a significant high tensile strength of more than 7000 psi, and operate very well at temperatures of more than 1300 °C. Such alloys have low thermal expansion coefficient and high oxidation resistance [35, 36]. Generally, the temperature difference among the junctions of two dissimilar metals can produce a low power closed-circuit electric current. In this case, Si and Ge can produce the current without external power sources. SiGe for n-leg and p-leg is doped with boron and phosphorus, respectively. Electrical and thermal currents are completely separated by a multifoil cold stack assembly of Cu, Al, Mo, W, and stainless steel components [37]. Also, layers of quartz silica fiber electrically insulate the thermocouples [38]. The schematic figure of the TEG design is presented in Figure 8.4.

Voyager power sources are still running, and it is expected to last for 35 years. A typical figure of an RTG module is presented in Figure 8.5. Voyager was equipped with multihundred-watt radioisotope thermoelectric generators (MHW-RTG) [39]. Each of the modules had a weight of 33.2 and 4.5 kg of Pu-238. By using 24 pressed plutonium-238 oxide spheres, it could produce an amount of heat for generating 157 W of electrical power for 87.7 years [40]. A total of 312 silicon–germanium (SiGe) TE couples were used, which could bear 1273 K on its hot side and 573 K on its cold side [37]. Three RTG modules were enough for the Voyager to provide this spacecraft with 470 W electrical power.

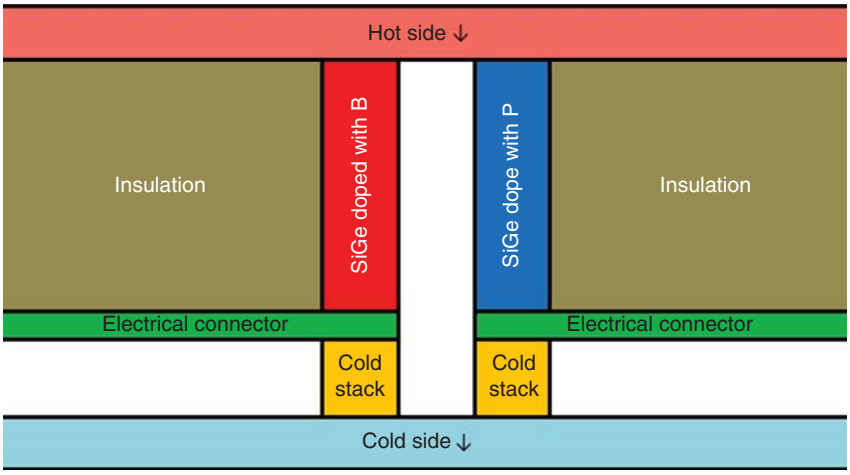

Figure 8.4 Schematic figure of the TEG design.

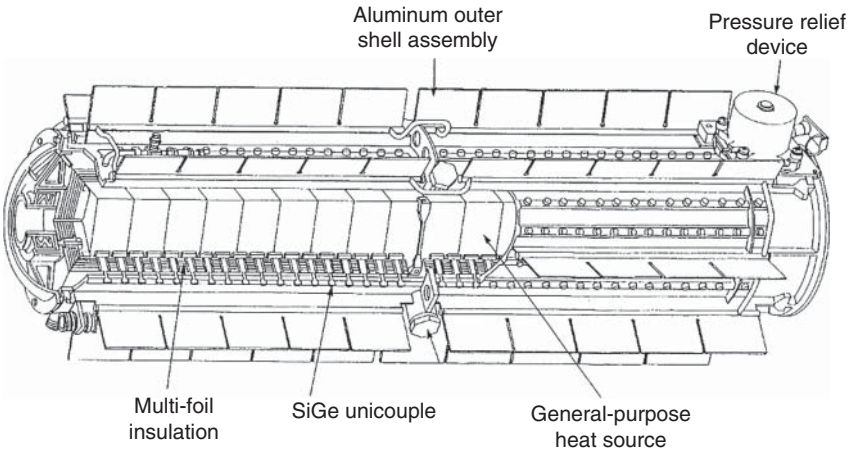

Figure 8.5 Radioisotope thermoelectric generator (RTG) [37].

Galileo (1989), Ulysses (1990), Cassini (1997), and the New Horizons (2006) all contained the general-purpose heat source (GPHS) RTG developed by the US Department of Energy [38].

For further distances and discoveries beyond Mars, the missions after 2010, multi-mission radioisotope thermoelectric generator (MMRTG) has been implemented. MMRTGs carry 106 lbs of Pu-238 and they can provide 110 W electricity power. Lead telluride (PbTe) is the main material for thermocouples, and the heat is generated from Pu-238 dioxide. The New Horizons spacecraft has passed Pluto in 2015, and its next destination is billion miles beyond Pluto. Table 8.1 illustrates the RTG space exploration timeline.

Table 8.1 RTG space exploration timeline.

Launch year	Mission	RTG	Destination	Length (years)
1976	LES8/LES9	MHW-RTG (4)	Earth orbit	15
1977	Voyager1/Voyager2	MHW-RTG (3)	Outer planets	31
1989	Galileo	GPHS-RTG (2)/RHU (120)	Outer planets	14
1990	Ulysses	GPHS-RTG (1)	Outer planets/Sun	18
1997	Cassini	GPHS-RTG (3)	Outer planets	11
2005	New Horizons	GPHS-RTG (1)	Outer planets	17

8.4 Thermoelectric Nanocomposites and Their Processing Methods

8.4.1 Bismuth Telluride, PbTe, SbTe, Etc.

Bi_2Te_3 is one of the most classical TE materials, which is widely used for TE cooling purpose. First reported as a Peltier cooler in 1954 by Goldsmid and Douglas [3], Bi_2Te_3 is a gray color compound of bismuth (Bi) and tellurium (Te). Bi_2Te_3 has a narrow bandgap of about 0.16 eV. It has a trigonal unit cell structure as shown in Figure 8.6. Blue balls stand for Te atoms and the red ones are Bi atoms.

Bi_2Te_3 is still the best material in low temperature range in terms of the TE figure of merit ZT. As shown in Figure 8.7, it is clear that n-type Bi_2Te_3 can reach a peak of ZT of 1.0 at 370 K (97 °C) and even higher for p-type Bi_2Te_3 due to its higher Seebeck coefficient.

However, there are a couple of drawbacks of Bi_2Te_3. First, Bi_2Te_3 may emit Te, which is highly toxic. Exposure to Te can cause a garlic-like smell when breathing, called tellurium breath. Second, Bi and Te are both trace metal, meaning that the price to produce Bi_2Te_3 is very expensive.

Antimony telluride (Sb_2Te_3) has the same crystal structure as Bi_2Te_3 in Figure 8.6, but with slightly different lattice constant: aBiTe = 4.384 Å, cBiTe = 30.487 Å, aSbTe = 4.264 Å, and cSbTe = 30.458 Å [43]. The optimal operational temperature of Sb_2Te_3 is around 500 K, where Sb_2Te_3 reaches its maximum ZT of 0.4 [44]. Identified along with Bi_2Te_3 by Werner Haken in 1910, lead telluride (PbTe) is also a popular TE material with high performance. However, PbTe is different compared to Bi_2Te_3 in many ways because it has a halite crystal structure, which is cubic-like sodium chloride, as shown in Figure 8.8. Pb atom is green, while Te atom is red. The lattice constant aPbTe is 6.456 Å.

With a slightly higher bandgap of around 0.3 eV, PbTe also has a higher temperature region for TE purpose. As shown in Figure 8.7, it has a peak ZT of 1.75 at 500 K, making it one of the best performance TE materials in the middle-temperature region. Typical values of TE properties for Bi_2Te_3, Sb_2Te_3, and PbTe are summarized in Table 8.2. PbTe also shares some similar problems

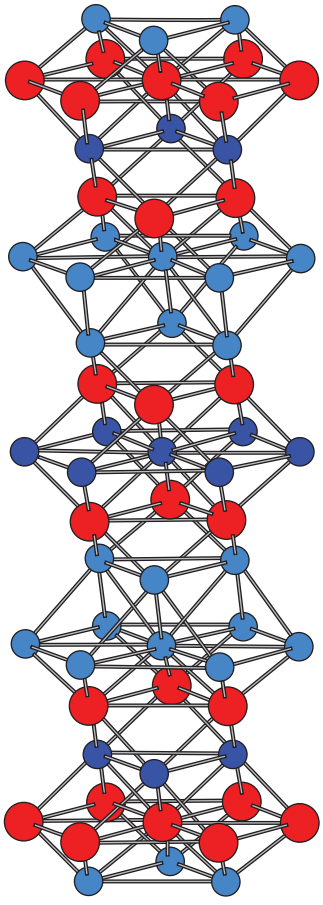

Figure 8.6 Crystal structure of Bi_2Te_3. (Bali *et al*. 2013 [41]. Reproduced with permission of American Institute of Physics.)

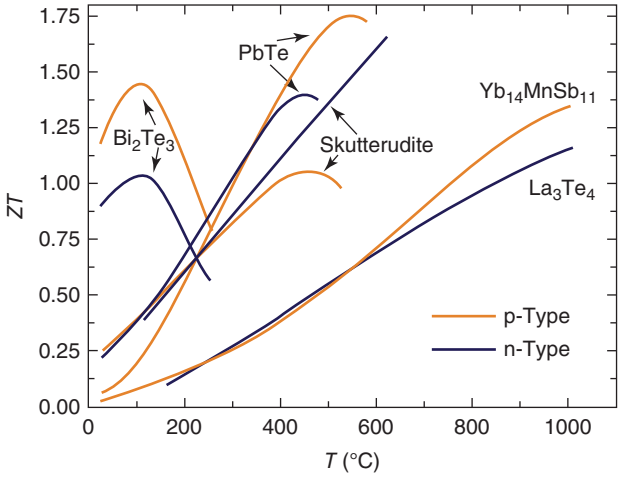

Figure 8.7 *ZT* values of different materials. (Baranowski *et al*. 2012 [42]. Reproduced with permission of Royal Society of Chemistry.)

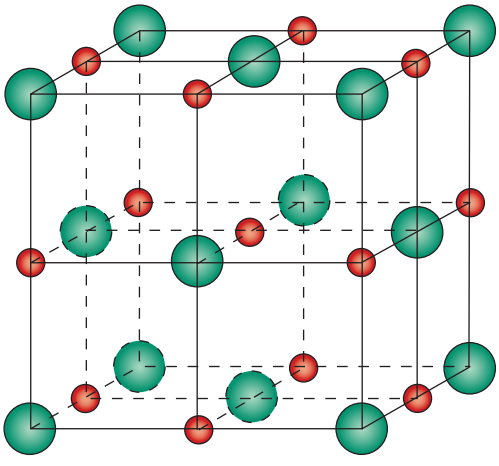

Figure 8.8 Crystal structure of PbTe [45].

Table 8.2 TE properties of Bi_2Te_3, Sb_2Te_3, and PbTe [41, 44, 46, 47].

Material	ρ (mΩ cm) (300 K)	S (μV/K) (300 K)	k (W/m K) (200 K)	ZT (300 K)
Bi_2Te_3	1.4	−180	2.0	0.35
Sb_2Te_3	0.69	125	2.5	0.27
PbTe	0.5	−40	2.24 (400 K)	0.2 (400 K)

with Bi_2Te_3. If PbTe is decomposed by heat or acid, it can emit lead salts. Lead is very toxic and lead poisoning can harm the nervous system. Depending on the quality of the material, PbTe can be even more expensive than Bi_2Te_3.

8.4.2 Emerging Materials: Silicides and Nitrides

Among the new materials under research for TE performance, silicides and nitrides are two promising candidates. Nitrides are compounds based on nitrogen, while silicides are based on silicon. Since nitrogen and silicon are abundant, cheap, and eco-friendly components, TE materials based on these components could be highly cost-effective.

Within the group of nitrides, the III-nitrides have been receiving especial attention [21]. These materials are composed of nitrogen and elements from the third column of the periodic table, such as aluminum, gallium, and indium. These materials are generally characterized by having strong chemical bonds, due to the large difference in electronegativity of these compounds and a wide direct bandgap [48]. III-Nitrides are generally characterized by its high temperature stability, high Seebeck coefficients, and PF. The challenge that is currently being investigated in these composites is their high thermal conductivity, which drastically reduces the overall ZT value.

In order to reduce thermal conductivity, phonon scattering in III-nitrides are often enhanced and increased by alloying [21]. For instance, InGaN has shown

promising TE properties compared with GaN due to its low thermal conductivity caused by enhanced phonon scattering. However, there is a paradox for this material: the crystal structure suffers from a high degeneration at high indium concentrations, so lattice mismatches happen, which brings undesirable effects in other properties as well, such as low electrical conductivity [21]. Silicides are considered promising TE materials due to their mechanical and chemical strength and high ZT values. These materials are suitable for operations in the range of 300–600 °C, which is the range for organic fuel burning [49]. Tani and Kido developed a Mg_2Si sample heavily doped with Bi and reached $ZT = 0.86$, at 862 K [50].

Figure 8.9 shows the PF from four different materials (MnSi, InGaN, AlInGaN, and SbTe), as reported by Pantha *et al.* [51], Sztein *et al.* [52], Chen *et al.* [53], and Silva *et al.* [54]. For the two nitrides and the silicide, it is possible to notice that the PF is consistently high at high temperatures, reaching values above 18×10^{-14} W/m K^2 for MnSi at temperatures above 800 K.

For the sample of Sb–Te, as plotted for comparison, we can observe a different behavior. Its PF is substantially high within the temperature range of 500–560 K but suffers a sharp decrease beyond that due to bipolar effect in narrow bandgap materials. For this reason, the Sb–Te composite can be an adequate choice for thermoelectricity in a lower temperature range, but it is not adequate for high temperature systems.

Further improvements are required in silicides and nitrides, especially to reduce thermal conductivity, in order to increase the figure of merit. However, because of the abovementioned advantages of these composites, if the figure of merit is successfully increased, they will become formidable candidates for mass production of TE devices for high temperature applications.

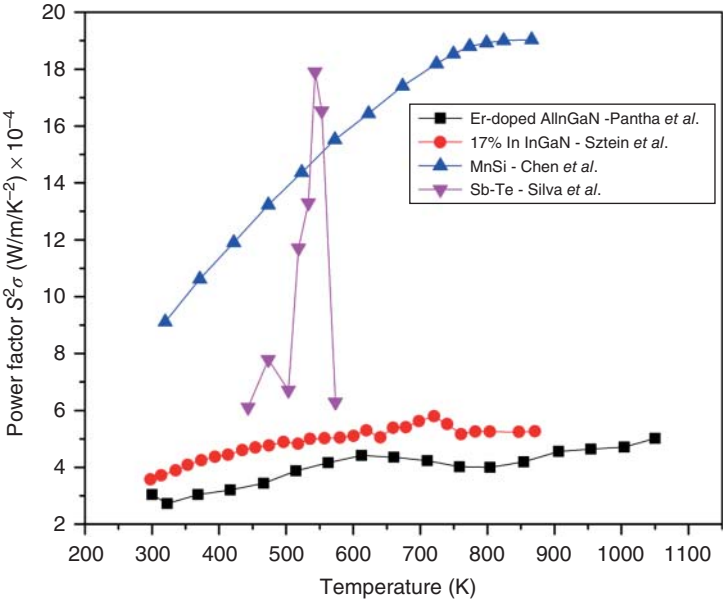

Figure 8.9 Power factor (PF) for three different materials, as reported by [51–54].

8.4.3 SiGe and Other RTG Materials

When it comes to TE materials used for commercial applications, SiGe holds the state-of-the-art position for high temperature applications, reaching $ZT = 0.9$ at 1200 K [55]. This material is already used for RTG by NASA for space missions, but its extremely high cost (~\$350–\$680 kg^{-1}) is hindering large-scale applications.

Table 8.3 compares the published data of TE performance of SiGe, nitrides, and oxides with conventional TE materials. As shown, conventional TE materials are not functional at temperatures above 1000 K. Moreover, the oxides and nitrides have two order of magnitude higher in PF and two order of magnitude reduction in materials cost [60] while being able to achieve higher operational temperatures than that of the conventional ones.

Table 8.4 summarizes the current status of different TE, including nitrides, oxides, skutterudites, and half-Heuslers, and the commercially used SiGe. For

Table 8.3 TE properties of nitrides and oxides versus commercial ones PbTe and SiGe.

Material	S (μV/K)	σ (Ω^{-1} cm^{-1})	k (W/m K)	PF (mW/m K^2)	ZT (300 K)	Maximum temperature (K)	Material cost ($/kg)
$Bi_{0.52}Sb_{1.48}Te_3$ [56]	238	600	0.67	0.30	1.52	400	125
$AgPb_mSbTe_{2+m}$ [57]	155	520	1.8	0.17	0.4	700	83
$Si_{0.8}Ge_{0.2}$ [58]	125	850	2.5	0.15	0.18	1000	630
$Zn_{0.95}Al_{0.05}O$ [59]	155	200	35	15.10	0.03	2000	0.60
$In_{0.07}Ga_{0.93}N$ [22]	507	85	11	21.84	0.07	2200	2.30

Table 8.4 Summary of state-of-the art TE materials.

Material type	Material name	Type	Material cost ($/kg)	ZT material	PF (μW/cm K^2)	References
SiGe	SiGe	Bulk	679	0.65	18	[58]
	$Si_{0.8}Ge_{0.2}$	Nanobulk	371	0.95	23	[58]
Silicides	$Mg_2Si_{0.85}Bi_{0.15}$	Nanobulk	6.67	0.7	33	[61]
	$Mg_2Si_{0.6}Sn_{0.4}$	Bulk	3.05	1.1	30	[62]
Skutterudites	$CeFe_4Sb_{12}$	Bulk	37	0.87	33	[63]
	$Yb_{0.2}In_{0.2}Co_4Sb_{12}$	Bulk	24	1	44.1	[64]
	$Ca_{0.18}Co_{3.97}Ni_{0.03}Sb_{12.4}$	Bulk	13	1	47	[65]
Half-Heuslers	$Zr_{0.25}Hf_{0.25}Ti_{0.5}NiSn_{0.994}Sb_{0.006}$	Nanobulk	9.1	1.5	52	[66]
	$Ti_{0.8}Hf_{0.2}NiSn$	Nanobulk	10.70	0.43	23	[67]
Nitrides	$In_{0.17}Ga_{0.83}N$	Thin film	2.30	0.34	1000	[52]
Oxides	$(Zn_{0.98}Al_{0.02})O$	Bulk	0.6	0.3	1500	[59]

silicides, skutterudites, and half-Heuslers, the operational temperature is typically lower than 800 K due to its narrow bandgap characteristics. Additionally, maintaining a consistent stoichiometry of skutterudites and half-Heuslers still remains challenging.

Nitrides and oxides have many advantages for large-scale high temperature waste heat harvesting applications, including low cost, nontoxic, earth abundance, high PF, and high temperature stability with melting temperature up to 2200 °C [68]. In addition, both nitrides and oxides are well-developed semiconductors with a mature device fabrication infrastructure for electronics and optoelectronics in high temperature applications, such as LED, solar cells, laser, photodiodes, and high power electronics. Therefore, normal technological difficulties in conventional TE devices, such as the formation of good electric contracts, are not expected in GaN and ZnO as they benefit from a mature existing device infrastructure. For instance, indium (In), titanium (Ti), gold (Au), and platinum (Pt) have been frequently used for making good high temperature contacts for these materials.

8.4.4 Oxide

In spite of the high TE efficiency of alloys such as Bi_2Te_3, PbTe, and $Si_{1-x}Ge_x$, they are low in abundance as natural resources and not environmentally friendly [69]. Also the thermal stability of these materials is poor. In contrast, there are some oxides with nontoxic elements that are promising for use in TE devices. The high thermal stability of oxides allows for a large temperature gradient to be applied across the materials. Also, oxides are beneficial in terms of the cost of raw materials and the environmental friendliness. The figures of merit for these materials are generally lower than those for alloys, but their thermal and chemical stability are better. The oxide TE materials can be divided into two main groups, which are described in the following.

8.4.4.1 n-Type Oxide ZnO-Based Materials

Zinc oxide (ZnO) is a wide bandgap semiconductor with a direct bandgap of 3.2–3.5 eV [70]. It is stable at high temperature, high electrical conductive by Al-doping, nontoxic, and low cost. These properties make it a potential candidate for n-type TE materials in high temperature applications [71, 72]. ZnO has a high thermal conductivity due to its noncomplex wurtzite structure, which heavily limits the interest in ZnO for TE application. Several attempts have been made to improve the TE properties of ZnO. The introduction of a second nanophase was found to be effective to decrease the thermal conductivity. In fact, by using natural phase separation and defined thermal treatment, the minor phase can be selectively induced to precipitate as nanoparticles [73]. Also the small amount of induced aluminum was found to be effective in reducing thermal conductivity [74]. The beneficial effect of aluminum has been attributed to aluminum, decreasing the *c*-to-*a* ratio of the crystal [75]. It has been reported that Al-induced grain refinement can enhance phonon scattering due to plenty of interfaces and defects, which results in a 2 W/m K and $ZT \sim 0.44$ at 1000 K [71].

Al- and Ga-doped ZnO are considered as the best n-type TE oxide materials. It has been reported that 2% Al-doped ZnO exhibits high TE performance: electrical conductivity $\sigma = 923$ S/cm and Seebeck coefficient $S = -111\,\mu$V/K at 600 K [76]. A significant enhancement of the TE PF in polycrystalline Ga-doped ZnO was reported. Jung *et al*. found that a single-phase n-type $Zn_{0.985}Ga_{0.015}O$ bulk exhibited a PF of 12.5 $\mu W/cm\,K^2$ [77].

8.4.4.2 p-Type Oxide

The cobaltite compound is the most promising p-type oxide TE materials, which have large Seebeck coefficients due to the low spin state of Co^{3+}. The structures of $Ca_3Co_4O_9$ oxides are shown schematically in Figure 8.10 [78] in which the CoO_2 planes are separated by a layer that forms a rock salt-type structure.

Although $Ca_3Co_2O_6$ has a large Seebeck coefficient, the conductivity is low, so $Ca_3Co_4O_9$ has been more widely used for TE applications. The most common dopant for $Ca_3Co_4O_9$ is bismuth, which has been proved to be effective in enhancing the electrical conductivity and Seebeck coefficient as well as decreasing the thermal conductivity. The decrease in thermal conductivity is due to the larger size and mass of bismuth as compared with those of calcium [79]. As discussed above, two types of oxide TE including p-type and n-type oxides are available to be used as a TE material for high temperature application. The p-type oxides with the best TE properties are layered cobaltite compounds due to better stability, while ZnO is among the most widely studied n-type oxides.

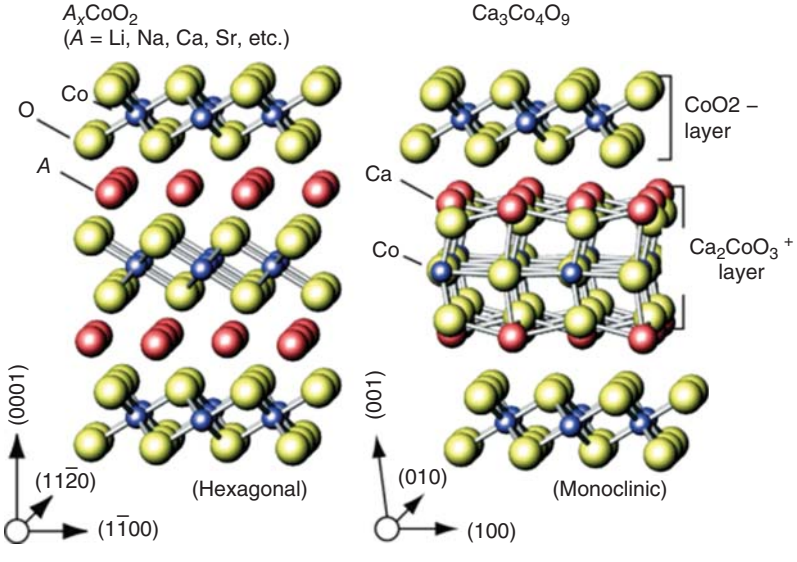

Figure 8.10 Schematic crystal structures of layered cobalt oxides. (a) A_xCoO_2 (A = Li, Na, Ca, Sr). (b) $Ca_3Co_4O_9$. Both crystals have CoO_2-layers composed of edge-shared CoO_6 octahedra. (Ohta *et al*. 2008 [78]. Reproduced with permission of John Wiley and Sons.)

8.5 Thermoelectric Device Design and Characterizations

8.5.1 Device Physics and Calculation

A typical TEG module is shown in Figure 8.11. It includes a number of basic p- and n-type TE elements connected electrically in series and thermally in parallel and sandwiched between two ceramic plates. For instance, a hybrid p–n structure of p-type InGaN/n-type ZnO can be produced due to their similar thermal expansion coefficients and lattice constant [80]. The compatibility will not be a concern since both InGaN and ZnO have similar TE properties.

As discussed before, material figure of merit is obtained according to Eq. (8.2). Therefore, the efficiency of a TE material is based on high electrical conductivity as well as low thermal conductivity. The output voltage (V) and current (I) of a TE device are given by Eqs (8.16) and (8.17):

$$V = \frac{N\alpha(T_h - T_c)}{1 + 2rl_c/l} \tag{8.16}$$

$$I = \frac{A\alpha(T_h - T_c)}{2\rho(n + 1)(1 + 2rl_c/l)} \tag{8.17}$$

where N is the number of thermocouples in a module, α is the Seebeck coefficient of the thermoelement material, ρ is the electrical resistivity, and T_h and T_c are temperatures at the hot and cold sides of the module, respectively. A and l are the cross-sectional area and TE length, respectively. l_c is the thickness of the contact layer, $n = 2\rho_c/\rho$, and $r = \lambda/\lambda_c$ (where ρ_c is the electrical contact resistivity, λ_c is the thermal contact conductivity, and λ is the thermal conductivity of thermoelement materials). n and r are usually referred to as electrical and thermal contact parameters, respectively. The power output P and conversion efficiency Φ of a TE module, when operated with a match load, can be

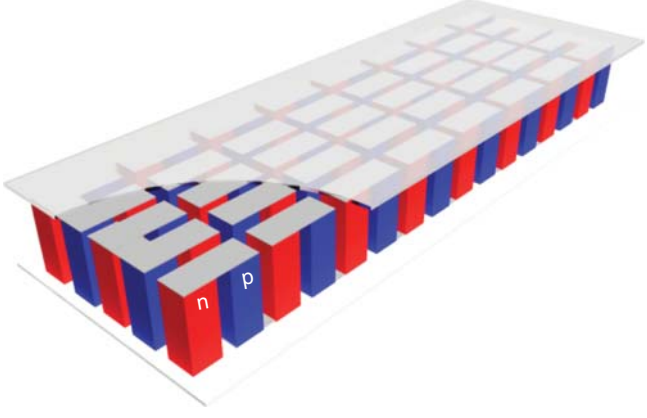

Figure 8.11 Schematic of a typical TEG module, which includes multiple p–n TE elements.

expressed as Eqs (8.18) and (8.19):

$$P = \frac{\alpha^2}{2\rho}\frac{AN(T_h - T_c)^2}{(n+l)(1+2rl_c/l)^2} \tag{8.18}$$

$$\Phi = \frac{\left(\frac{T_h - T_c}{T_h}\right)}{\left(1+2r\frac{l_c}{l}\right)^2\left[2 - \frac{1}{2}\left(\frac{T_h - T_c}{T_h}\right) + \left(\frac{4}{ZT_h}\right)\left(\frac{1+n}{1+2rl_c}\right)\right]} \tag{8.19}$$

where $Z = \alpha^2/(\rho\lambda)$ is the TE figure of merit of the materials.

The maximum efficiency (η_{max}) of a TE material is related to two variables. The first one is called the thermoelectric figure of merit (ZT), which depends on the Seebeck coefficient (α), electrical resistivity (ρ), and thermal conductivity (k). The second term is the Carnot efficiency (Eq. (8.20)) and, for all heat engines, the maximum efficiency does not exceed this value.

$$\eta_{max} = \frac{\Delta T}{T_h}\cdot\frac{\sqrt{1+ZT}-1}{\sqrt{1+ZT}+1} \tag{8.20}$$

where T_h is the maximum temperature at the hot side (K), ΔT is the temperature difference on both sides (K), and ZT is the figure of merit. The power output (mW) for 1 cm^2 TEG module is presented in Figure 8.12.

The Seebeck coefficient is 470 (μV/K), electrical conductivity is 400 (S/m), and thermal conductivity is 22 (W/m K). The temperature at the cold and hot sides is 500 and 1300 K, respectively. The dimension of one n–p leg is $1 \times 3 \times 1$ mm^3. The fill factor is chosen 0.8 in this calculation.

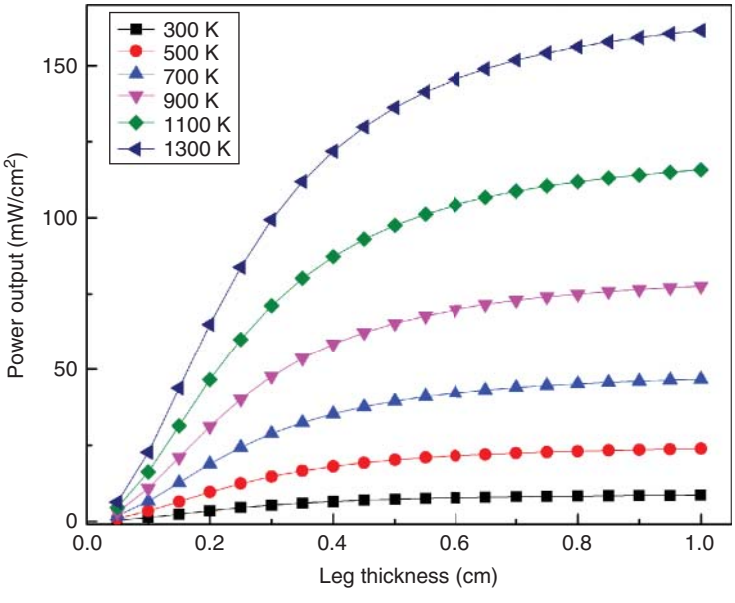

Figure 8.12 The power output (mW) for 1 cm^2 TEG module.

8.5.2 TE Device Fabrication and Its Applications

Several methods of flexible TEG fabrication have been proposed. Micromachine thermopile is one of the methods, which are discussed in the following. The poly-SiGe-based thermopile can be fabricated by using surface micromachining technology. Shallow trenches as deep as 2.5 m is etched into an 8″ Si substrate. On top of the layer, a thin Si_3N_4 layer is deposited for encapsulation. In situ doped p-type and n-type poly-SiGe layers are deposited by low temperature chemical vapor deposition (LPCVD) afterward and then patterned by photolithography and dry etch, respectively, to shape the thermocouple legs. Next, the poly-SiGe layer surface is thoroughly cleaned with argon plasma, immediately succeeded by aluminum sputtering and patterning to interconnect thermocouple legs electrically. Finally, the thermopile chip is released in BHF solution and dried with critical point dryer to avoid sticking [81].

Organic materials, hybrid composites, and paste-type materials are preferred because of their soft phase. In addition, solution-processability is a key to scalable and cost-effective fabrication of TEGs. Polymer-based materials have significantly low thermal conductivities, they can easily reach high electrical conductivities by being doped, and such lightweight materials are earth abundant [82, 83]. However, for instance, poly(3,4-ethylenedioxythiophene) (PEDOT) ZT value has been reported 0.2–0.4, which is significantly lower than those of inorganic TEG modules [84, 85]. The legs can be formed by pressing the polymer powder into pellets. The organic TEG is thus not a micro-thermogenerator but a robust device for higher power generation. The top and bottom sides of the pellets are coated with a thin Au layer in order to enable a better contact with the interconnects during the module assembly [82].

Table 8.5 summarizes the current status of different TE, including nitrides and oxides. Among them, SiGe is commercially available and used for RTG by NASA for space missions, as discussed before. But they are extremely high cost (~\$350–\$680 kg^{-1}), which hinders their large-scale application. For silicides, skutterudites, and half-Heuslers, the operational temperature is typically lower than 800 K due to its narrow bandgap characteristics. Additionally, maintaining a consistent stoichiometry of skutterudites and half-Heuslers still remains challenging.

Scalable fabrication of flexible TE devices has recently been given much attention for wearable energy-harvesting purposes. Screen printing, inkjet printing, molding, lithography, and vacuum deposition are among the methods of fabrication of flexible TE devices. Summary of the state-of-the-art TE materials is presented in Table 8.6. The most widely used method of TEG fabrication is screen printing. In this method, ink is cast onto a flexible substrate, which is covered by a mask [94]. Another advantage of screen printing is its scalability and mass productibility. When coupled with the roll-to-roll process, meter-long modules containing 18 000 TE are manufactured [95]. Inkjet printing method works similar to what a normal inkjet printer does: design pattern is sketched in a controlling computer, the ink cartridge is filled with TE material, and the materials are dispensed on the preferred substrate following the pattern. Less human labor, material waste, and precision are of the most important advantages of this

Table 8.5 Summary of state-of-the-art TE materials for mid- to high-temperature applications.

Material type	Material name	Type	Material cost ($/kg)	Evaluated for low or high temperature scenario			References
				ZT_m material	PF ($\mu W/cm\,K^2$)	Scenario Temperature (K)	
SiGe	SiGe	Bulk	679	0.65	18	1073	[58]
	$Si_{80}Ge_{20}$	Nanobulk	371	0.95	23	1173	[58]
Silicides	$Mg_2Si_{0.85}Bi_{0.15}$	Nanobulk	6.67	0.7	33	655	[61]
	$Mg_2Si_{0.6}Sn_{0.4}$	Bulk	3.05	1.1	30	700	[62]
Skutterudites	$CeFe_4Sb_{12}$	Bulk	37	0.87	33	750	[63]
	$Yb_{0.2}In_{0.2}Co_4Sb_{12}$	Bulk	24	1	44.1	750	[64]
	$Ca_{0.18}Co_{3.97}Ni_{0.03}Sb_{12.4}$	Bulk	13	1	47	800	[65]
Half-Heuslers	$Zr_{0.25}Hf_{0.25}Ti_{0.5}NiSn_{0.994}Sb_{0.006}$	Nanobulk	9.1	1.5	52	700	[66]
	$Ti_{0.8}Hf_{0.2}NiSn$	Nanobulk	10.70	0.43	23	670	[67]
Nitrides	$\mathbf{In_{0.17}Ga_{0.83}Ns}$	**Thin film**	**2.30**	**0.34**	**1000**	**900**	[59]
Oxides	$\mathbf{(Zn_{0.98}Al_{0.02})O}$	**Bulk**	**0.6**	**0.3**	**1500**	**1273**	[59]

Table 8.6 Summary of state-of-the-art TE materials.

Methods	Materials		Thickness (μm)	ΔT (K)	P_{max}	References
	n-Type	p-Type				
Screen printing	Bi_2Te_3/epoxy	Sb_2Te_3/epoxy	500	50	10.5	[86]
	Bi_2Te_3/epoxy	Sb_2Te_3/epoxy	40	50	12	[87]
	Bi_2Te_3/epoxy	Sb_2Te_3/epoxy	65	20	0.19	[88]
Inkjet printing	Bi_2Te_3/epoxy	Sb_2Te_3/epoxy	500	30	2	[89]
	Bi/epoxy	$Bi_{0.5}Sb_{1.5}Te_3$/epoxy	120	70	130	[90]
Molding	$Bi_2Te_{3-x}Se_x$/epoxy	$Bi_{0.5}Sb_{1.5}Te_3$/epoxy	4000	25	5	[91]
Lithography	Bi_2Te_3	Sb_2Te_3	30	10	0.13	[84]
Vacuum deposition	Bi_2Te_3	Sb_2Te_3	0.7	34	55	[92]
	$Bi_2Te_{2.7}Se_{0.3}$	$Bi_{0.4}Sb_{1.6}Te_3$	1	130	100	[93]

fabrication method. One drawback in this method is the micrometer thickness of the films. For wearable energy-harvesting maximum output, TE modules that take advantage of temperature gradient in the cross-plane direction are suitable. This means that the inkjet printer TE elements are limited to in-plane direction temperature gradient due to which leads to a considerable low output. By following molding and lithography methods, such problem would not exist. Molded PDMS membranes with arrays of cavities filled with TE materials have been manufactured [91]. The thickness is in millimeters, which gives a significant temperature difference in the cross-plane direction. Making thicker films by printing multiple times can also help in reducing the resistance of TE elements [87]. Photolithography technique is another method of TEG module fabrication. In this process, cavities are created in a photoresist SU-850, and then by using the inkjet printing method materials are dispensed into the cavities, which potentiates the large-scale manufacturing [84]. Deposition of Ni between Bi_2Te_3 and Sb_2Te_3 epoxy and electrodes can decrease the internal resistance to less than 1 Ω [86], which will lead to a higher power output. Furthermore, high temperature (250–350 °C) annealing is required after the manufacturing processes, which may lead to a high process cost. Development of new high ZT organic materials with low temperature scalable processes still remains a major challenge. In SMART Lab at Purdue University, ZnO and InGaN are implemented as p–n junctions. Nitrides and oxides have many advantages for large-scale high temperature waste heat harvesting applications, including low cost, nontoxic, earth abundance, high PF, and high temperature stability with melting temperature up to 2200 °C [68]. In addition, both nitrides and oxides are well-developed semiconductors with a mature device fabrication infrastructure for electronics and optoelectronics in high temperature applications, such as LED, solar cells, laser, photodiodes, and high power electronics. Therefore, normal technological difficulties in conventional TE devices, such as the formation of good electric contracts, are not expected in GaN and ZnO as they benefit from a mature existing device

infrastructure. For instance, indium (In), titanium (Ti), gold (Au), and platinum (Pt) have been frequently used for making good high temperature contacts for these materials.

References

1 Chen, Z., Han, G., Yang, L., Cheng, L., and Zou, J. (2012) Nanostructured thermoelectric materials: current research and future challenge. *Prog. Nat. Sci. Mater. Int.*, **22**, 15.
2 Tritt, T.M. and Subramanian, M.A. (2006) Thermoelectric materials, phenomena, and applications: a bird's eye view. *MRS Bull.*, **31**, 7.
3 Goldsmid, H.J. and Douglas, R.W. (1954) The use of semiconductors in thermoelectric refrigeration. *Br. J. Appl. Phys.*, **5**, 386.
4 Dresselhaus, M.S., Chen, G., Tang, M.Y., Yang, R., Lee, H., Wang, D.Z., Ren, Z.F., Fleurial, J., and Gogna, P. (2007) New directions for low-dimensional thermoelectric materials. *Adv. Mater.*, **19**, 11.
5 Alam, H. and Ramakrishna, S. (2013) A review on the enhancement of figure of merit from bulk to nano-thermoelectric materials. *Nano Energy*, **2**, 13.
6 Riffat, S. and Ma, X. (2003) Thermoelectrics: a review of present and potential applications. *Appl. Therm. Eng.*, **23**, 23.
7 Tie, S. and Tan, C.W. (2013) A review of energy sources and energy management system in electric vehicles. *Renewable Sustainable Energy Rev.*, **20**, 21.
8 Ullah, K., Saidur, R., Ping, H.W., Akikur, R.K., and Shuvo, N.H. (2013) A review of solar thermal refrigeration and cooling methods. *Renewable Sustainable Energy Rev.*, **24**, 15.
9 Pichanusakorn, P. and Bandaru, P. (2010) Nanostructured thermoelectrics. *Mater. Sci. Eng., R*, **67**, 45.
10 Gillispie, C.C. (1970) *Dictionary of Scientific Biography*, p. 16.
11 Seebeck, T.J. (1826) Ueber Die Magnetische Polarisation Der Metalle Und Erze Durch Temperatur-Differenz. *Ann. Phys.*, **82**, 133–160.
12 1907) *The New Werner Twentieth Century Edition of the Encyclopaedia Britannica: A Standard Work of Reference in Art, Literature, Science, History, Geography, Commerce, Biography, Discovery and Invention*, Werner Company.
13 Patil, P. and Patil, A. (2013) Review on thermoelectric devices. *Int. J. Emerg. Technol. Adv. Eng.*, **3**, 681–688.
14 Skripnik, Y.A. and Khimicheva, A.I. (1997) Methods and devices for measuring the Peltier coefficient of an inhomogeneous electric circuit. *Meas. Tech.*, **40**, 673–677.
15 Robertson, E.F. and O'Conner, J.J.. 2005 Biography of William Thomson (Lord Kelvin), http://www-history.mcs.st-andrews.ac.uk/Biographies/Thomson.html (accessed 8 May).
16 Rowe, D.M. (2005) *Thermoelectrics Handbook: Macro to Nano*, CRC Press.
17 Tian, Z., Lee, S., and Chen, G. (2014) A comprehensive review of heat transfer in thermoelectric materials and devices. *ARXIV*, **64**.
18 Lundstrom, M. and Jeong, C. (2013) *Near-Equilibrium Transport: Fundamentals and Applications*, vol. **2**, World Scientific.

19 Maris, H.J. and Tamura, S.-I. (2012) Heat flow in nanostructures in the Casimir regime. *Phys. Rev. B*, **85**, 054304.

20 Tong, T., Fu, D., Levander, A.X., Schaff, W.J., Pantha, B.N., Lu, N., Liu, B., Ferguson, I., Zhang, R., and Lin, J.Y. (2013) Suppression of thermal conductivity in Inxga$_{1-X}$n alloys by nanometer-scale disorder. *Appl. Phys. Lett.*, **102**, 121906.

21 Lu, N. and Ferguson, I. (2013) III-nitrides for energy production: photovoltaic and thermoelectric applications. *Semicond. Sci. Technol.*, **28**, 074023.

22 Kucukgok, B., Wu, X., Wang, X., Liu, Z., Ferguson, I.T., and Lu, N. (2016) The structural properties of ingan alloys and the interdependence on the thermoelectric behavior. *AIP Adv.*, **6**, 025305.

23 Bahk, J.-H. and Shakouri, A. (2014) Enhancing the thermoelectric figure of merit through the reduction of bipolar thermal conductivity with heterostructure barriers. *Appl. Phys. Lett.*, **105**, 052106.

24 Joffe, A.F. and Stil'bans, L.S. (1959) Physical problems of thermoelectricity. *Rep. Prog. Phys.*, **22**, 167.

25 Minnich, A.J., Dresselhaus, M.S., Ren, Z.F., and Chen, G. (2009) Bulk nanostructured thermoelectric materials: current research and future prospect. *Energy Environ. Sci.*, **2**, 14.

26 Rowe, D.M. and Bhandari, C.M. (1983) *Modern Thermoelectric*, Reston Publishing Company, Inc..

27 Vedernikov, M.V. and Iordanishvili, E.K. (1998) A.F. Ioffe and origin of modern semiconductor thermoelectric energy conversion. XVII International Conference on Thermoelectris.

28 Slack, G.A. (1995) New materials and performance limits for thermoelectric cooling, in *CRC Handbook of Thermoelectrics*, CRC Press.

29 Wu, D., Petersen, A.S., and Poon, S.J. (2013) Effective scattering cross-section in lattice thermal conductivity calculation with differential effective medium method. *AIP Adv.*, **3**, 082116.

30 Zide, J.M.O., Vashaee, D., Bian, Z.X., Zeng, G., Bowers, J.E., Shakouri, A., and Gossard, A.C. (2006) Demonstration of electron filtering to increase the Seebeck coefficient in In[0.53] Ga[0.47] As/In[0.53] Ga[0.28]Al [0.19]as superlattices. *Phys. Rev. B*, **74**, 205335.

31 Rull-Bravo, M., Moure, A., Fernandez, J.F., and Martin-Gonzalez, M. (2015) Skutterudites as thermoelectric materials: revisited. *RSC Adv.*, **5**, 41653–41667.

32 Hicks, L.D. and Dresselhaus, M.S. (1993) Effect of quantum-well structures on the thermoelectric figure of merit. *Phys. Rev. B*, **47**.

33 Raag, V. and Berlin, R.E. (1968) A silicon-germanium solar thermoelectric generator. *Energy Convers.*, **8**, 161–168.

34 Lee, E.K. *et al.* (2012) Large thermoelectric figure-of-merits from sige nanowires by simultaneously measuring electrical and thermal transport properties. *Nano Lett.*, **12**, 2918–2923.

35 Xie, M. and Gruen, D.M. (2010) Potential impact of Zt = 4 thermoelectric materials on solar thermal energy conversion technologies. *J. Phys. Chem. B*, **114**, 14339–14342.

36 Jurgensmeyer, A.L. (2011) *High Efficiency Thermoelectric Devices Fabricated Using Quantum Well Confinement Techniques*, Colorado State University, Ann Arbor, MI.

37 Furlong, R. and Wanhlquist, E. (1999) U.S. space missions using radioisotope power systems. *Nucl. News*, **42**, 26–34.

38 Sanchez-Torres, A. (2011) in *Radioisotope Power Systems for Space Applications* (ed. P.N. Singh), InTech.

39 Heacock, R. (1980) *The Voyager Spacecraft. James Watt International Gold Medal Lecture*, vol. **194**, The Institution of Mechanical Engineers, pp. 267–270.

40 Bennett, G. (2006) Space nuclear power: opening final frontier. 4th International Energy Conversion Engineering Conference and Exhibit (IECEC), San Diego, CA.

41 Bali, A., Chetty, R., and Mallik, R.C. (2013) Thermoelectric properties of PbTe with encapsulated bismuth secondary phase. *J. Appl. Phys.*, **113**, 9.

42 Baranowski, L.L.S., Jeffrey, G., and Toberer, E.S. (2012) Concentrated solar thermoelectric generators. *Energy Environ. Sci.*, **5**, 13.

43 Yavorsky, B.Y., Hinsche, N.F., Zahn, P., and Mertig, I. (2011) Electronic structure and transport anisotropy of Bi_2te_3 and Sb_2Te_3. *Phys. Rev. B*, **84**, 13.

44 Hu, L.P., Zhu, T.J., Yue, X.Q., Liu, X.H., Wang, Y.G., Xu, Z.J., and Zhao, X.B. (2014) Enhanced figure of merit in antimony telluride thermoelectric materials by in-Ag Co-alloying for mid-temperature power generation. *Acta Mater.*, **85**, 9.

45 Callister, W.D. and Rethwisch, D.G. (2011) *Fundementals of Materials Science and Engineering: An Integrated Approach*, 4th edn, John Wiley & Sons, Inc., p. 910.

46 Rosi, F.D., Abeles, B., and Jensen, R.V. (1959) Materials for thermoelectric refrigeration. *J. Phys. Chem. Solids*, **10**, 10.

47 Bos, J.W.G., Zandbergen, H.W., Lee, M.-H., Ong, N.P., and Cava, R.J. (2007) The structures and thermoelectric properties of the infinitely adaptive series (Bi_2) M (Bi_2Te_3) N. *Phys. Rev. B*, **75**, 33.

48 Kung, P. (2005) in *Optoelectronic Devices: III Nitrides* (eds M. Henini and M. Razeghim), Elsevier, Oxford, pp. 9–22.

49 Mikhail, I.F. and Grigory, N.I. (2015) Silicides: materials for thermoelectric energy conversion. *Jpn. J. Appl. Phys.*, **54**, 07JA05.

50 Tani, J.-I. and Kido, H. (2005) Thermoelectric properties of Bi-doped Mg_2si semiconductors. *Physica B*, **364**, 218–224.

51 Pantha, B.N., Feng, I.-W., Aryal, K., Li, J., Lin, J.-Y., and Jiang, H.-X. (2011) Erbium-doped alingan alloys as high-temperature thermoelectric materials. *Appl. Phys Express*, **4**.

52 Sztein, A., Ohta, H., Bowers, J.E., DenBaars, S.P., and Nakamura, S. (2011) High temperature thermoelectric properties of optimized InGaN. *J. Appl. Phys.*, **110**, 123709.

53 Chen, X., Zhou, J., Goodenoughab, J.B., and Shi, L. (2015) Enhanced thermoelectric power factor of re-substituted higher manganese silicides with small islands of MnSi secondary phase. *J. Mater. Chem. C*, **3**.

54 Silva, L.W.D., Kaviany, M., and Uher, C. (2005) Thermoelectric performance of films in the bismuth-tellurium and antimony-tellurium systems. *J. Appl. Phys.*, **97**.

55 Tritt, T.M. and Subramanian, M.A. (2006) Thermoelectric materials, phenomena, and applications: a bird's eye view. *MRS Bull.*, **31**, 188–198.

56 Xie, W., Tang, X., Yan, Y., Zhang, Q., and Tritt, T.M. (2009) High thermoelectric performance bisbte alloy with unique low-dimensional structure. *J. Appl. Phys.*, **105**, 113713.

57 Hsu, K.F., Loo, S., Guo, F., Chen, W., Dyck, J.S., Uher, C., Hogan, T., Polychroniadis, E.K., and Kanatzidis, M.G. (2004) Cubic $AgPb_mSbTe_{2+m}$: bulk thermoelectric materials with high figure of merit. *Science*, **303**, 818–821.

58 Joshi, G. *et al.* (2008) Enhanced thermoelectric figure-of-merit in nanostructured P-type silicon germanium bulk alloys. *Nano Lett.*, **8**, 4670–4674.

59 Tsubota, T., Ohtaki, M., Eguchi, K., and Arai, H. (1997) Thermoelectric properties of Al-doped Zno as a promising oxide material for high-temperature thermoelectric conversion. *J. Mater. Chem.*, **7**, 85–90.

60 LeBlanc, S., Yee, S.K., Scullin, M.L., Dames, C., and Goodson, K.E. (2014) Material and manufacturing cost considerations for thermoelectrics. *Renewable Sustainable Energy Rev.*, **32**, 313–327.

61 Bux, S.K., Yeung, M.T., Toberer, E.S., Snyder, G.J., Kaner, R.B., and Fleurial, J.-P. (2011) Mechanochemical synthesis and thermoelectric properties of high quality magnesium silicide. *J. Mater. Chem.*, **21**, 12259–12266.

62 Zaitsev, V.K., Fedorov, M.I., Gurieva, E.A., Eremin, I.S., Konstantinov, P.P., Samunin, A.Y., and Vedernikov, M.V. (2006) Highly effective thermoelectrics. *Phys. Rev. B*, **74**, 045207.

63 Qiu, P.F., Yang, J., Liu, R.H., Shi, X., Huang, X.Y., Snyder, G.J., Zhang, W., and Chen, L.D. (2011) High-temperature electrical and thermal transport properties of fully filled skutterudites RFe_4Sb_{12} (R = Ca, Sr, Ba, La, Ce, Pr, Nd, Eu, and Yb). *J. Appl. Phys.*, **109**, 063713.

64 Peng, J., He, J., Alboni, P.N., and Tritt, T.M. (2009) Synthesis and thermoelectric properties of the double-filled skutterudites $Yb_{0.2}$lny Co_4Sb_{12}. *J. Electron. Mater.*, **38**, 981–984.

65 Puyet, M., Dauscher, A., Lenoir, B., Dehmas, M., Stiewe, C., Müller, E., and Hejtmanek, J. (2005) Beneficial effect of Ni substitution on the thermoelectric properties in partially filled $Ca_yCo_{4-X}Ni_xSb_{12}$ skutterudites. *J. Appl. Phys.*, **97**, 083712.

66 Sakurada, S. and Shutoh, N. (2005) Effect of Ti substitution on the thermoelectric properties of (Zr,Hf)NiSn half-Heusler compounds. *Appl. Phys. Lett.*, **86**, 082105.

67 Katayama, T., Kim, S.W., Kimura, Y., and Mishima, Y. (2003) The effects of quaternary additions on thermoelectric properties of TiNiSn-based half-Heusler alloys. *J. Electron. Mater.*, **32**, 1160–1165.

68 Alexander, S., Hiroaki, O., Junichi, S., Ashok, R., John, E.B., Steven, P.D., and Shuji, N. (2009) GaN-based integrated lateral thermoelectric device for micro-power generation. *Appl. Phys Express*, **2**, 111003.

69 Nag, A. and Shubha, V. (2014) Oxide thermoelectric materials: a structure–property relationship. *J. Electron. Mater.*, **43**, 962–977.

70 Ohtaki, M. (2011) Recent aspects of oxide thermoelectric materials for power generation from mid-to-high temperature heat source. *J. Ceram. Soc. Jpn.*, **119**, 770–775.

71 Jood, P., Mehta, R.J., Zhang, Y., Peleckis, G., Wang, X., Siegel, R.W., Borca-Tasciuc, T., Dou, S., and Ramanath, G. (2011) Al-doped zinc oxide nanocomposites with enhanced thermoelectric properties. *Nano Lett.*, **11**, 4337–4342.

72 Ma, N., Li, J.F., Zhang, B.P., Lin, Y.H., Ren, L.R., and Chen, G.F. (2010) Microstructure and thermoelectric properties of $Zn_{1-X}Al_xO$ ceramics fabricated by spark plasma sintering. *J. Phys. Chem. Solids*, **71**, 1344–1349.

73 He, J., Kanatzidis, M.G., and Dravid, V.P. (2013) High performance bulk thermoelectrics via a panoscopic approach. *Mater. Today*, **16**, 166–176.

74 Guilmeau, E., Maignan, A., and Martin, C. (2009) Thermoelectric oxides: effect of doping in delafossites and zinc oxide. *J. Electron. Mater.*, **38**, 1104–1108.

75 Wiff, J.P., Kinemuchi, Y., Kaga, H., Ito, C., and Watari, K. (2009) Correlations between thermoelectric properties and effective mass caused by lattice distortion in Al-doped Zno ceramics. *J. Eur. Ceram. Soc.*, **29**, 1413–1418.

76 Shrikant, S., Paolo, M., Hiroaki, H., Dave, J.H., Patrick, E.H., Leopoldo, M., Kaname, M., Koji, M., and Ataru, I. (2014) Enhanced thermoelectric performance of Al-doped Zno thin films on amorphous substrate. *Jpn. J. Appl. Phys.*, **53**, 060306.

77 Jung, K., Hyoung, L., Seo, W., and Choi, S. (2012) An enhancement of a thermoelectric power factor in a Ga-doped Zno system: a chemical compression by enlarged Ga solubility. *Appl. Phys. Lett.*, **100**, 253902.

78 Ohta, H., Sugiura, K., and Koumoto, K. (2008) Recent progress in oxide thermoelectric materials: P-type $Ca_3Co_4O_9$ and N-type $SrTio_3^-$. *Inorg. Chem.*, **47**, 8429–8436.

79 Li, S., Funahashi, R., Matsubara, I., Ueno, K., Sodeoka, S., and Yamada, H. (2000) Synthesis and thermoelectric properties of the new oxide materials $Ca_{3-X}Bi_xCo_4O_{9+\Delta}$ $(0.0 < X < 0.75)$. *Chem. Mater.*, **12**, 2424–2427.

80 Wang, T., Wu, H., Wang, Z., Chen, C., and Liu, C. (2012) Improvement of optical performance of ZnO/GaN P-N junctions with an InGaN interlayer. *Appl. Phys. Lett.*, **101**, 161905.

81 Wang, Z., Leonov, V., Fiorini, P., and Van Hoof, C. (2009) Realization of a wearable miniaturized thermoelectric generator for human body applications. *Sens. Actuators, A*, **156**, 95–102.

82 Bubnova, O. and Crispin, X. (2012) Towards polymer-based organic thermoelectric generators. *Energy Environ. Sci.*, **5**, 9345–9362.

83 Chen, Y., Zhao, Y., and Liang, Z. (2015) Solution processed organic thermoelectrics: towards flexible thermoelectric modules. *Energy Environ. Sci.*, **8**, 401–422.

84 Bubnova, O., Khan, Z.U., Malti, A., Braun, S., Fahlman, M., Berggren, M., and Crispin, X. (2011) Optimization of the thermoelectric figure of merit in the conducting polymer poly(3,4-ethylenedioxythiophene). *Nat. Mater.*, **10**, 429–433.

85 Kim, G.H., Shao, L., Zhang, K., and Pipe, K.P. (2013) Engineered doping of organic semiconductors for enhanced thermoelectric efficiency. *Nat. Mater.*, **12**, 719–723.

86 Kim, S.J., We, J.H., and Cho, B.J. (2014) A wearable thermoelectric generator fabricated on a glass fabric. *Energy Environ. Sci.*, **7**, 1959–1965.

87 We, J.H., Kim, S.J., and Cho, B.J. (2014) Hybrid composite of screen-printed inorganic thermoelectric film and organic conducting polymer for flexible thermoelectric power generator. *Energy*, **73**, 506–512.

88 Cao, Z., Koukharenko, E., Tudor, M., Torah, R., and Beeby, S. (2013) Screen printed flexible Bi_2Te_3-Sb_2Te_3 based thermoelectric generator. *J. Phys. Conf. Ser.*, IOP Publishing:, **476**, 012031.

89 Kim, M.K., Kim, M.S., Jo, S., Kim, H., Lee, S., and Kim, Y.J. (2013) Wearable thermoelectric generator for human clothing applications. 2013 Transducers & Eurosensors XXVII: The 17th International Conference on Solid-State Sensors, Actuators and Microsystems (TRANSDUCERS & EUROSENSORS XXVII), IEEE, 2013, pp 1376-1379.

90 Madan, D., Wang, Z., Chen, A., Winslow, R., Wright, P.K., and Evans, J.W. (2014) Dispenser printed circular thermoelectric devices using Bi and $Bi_{0.5}Sb_{1.5}Te_3$. *Appl. Phys. Lett.*, **104**, 013902.

91 Jo, S.E., Kim, M.K., Kim, M.S., and Kim, Y.J. (2012) Flexible thermoelectric generator for human body heat energy harvesting. *Electron. Lett*, **48**, 1013–1015.

92 Baba, S., Sato, H., Huang, L., Uritani, A., Funahashi, R., and Akedo, J. (2014) Formation and characterization of polyethylene terephthalate-based $(Bi_{0.15}Sb_{0.85})2Te_3$ thermoelectric modules with $CoSb_3$ adhesion layer by aerosol deposition. *J. Alloys Compd.*, **589**, 56–60.

93 Mizue, M., Masashi, M., and Kimihiro, O. (2013) P-type Sb_2Te_3 and N-type Bi_2Te_3 films for thermoelectric modules deposited by thermally assisted sputtering method. *Jpn. J. Appl. Phys.*, **52**, 06GL07.

94 Wei, Q., Mukaida, M., Kirihara, K., Naitoh, Y., and Ishida, T. (2014) Polymer thermoelectric modules screen-printed on paper. *RSC Adv.*, **4**, 28802–28806.

95 Søndergaard, R.R., Hösel, M., Espinosa, N., Jørgensen, M., and Krebs, F.C. (2013) Practical evaluation of organic polymer thermoelectrics by large-area R2R processing on flexible substrates. *Energy Sci. Eng.*, **1**, 81–88.